Journal of Alloys and Compounds 904 (2022) 163976

Contents lists available at ScienceDirect

Journal of Alloys and Compounds

journal homepage: www.elsevier.com/locate/jalcom

Effect of sintering under $CO+N_2/H_2$ and CO_2+air atmospheres on the physicochemical features of a commercial nano-YSZ

M.T. Colomer[a,*], M. Simenas[b], J. Banys[b], F. Vattier[c], A. Gagor[d], M. Maczka[d]

[a] Instituto de Cerámica y Vidrio, CSIC, c/ Kelsen 5, E-28049 Madrid, Spain
[b] Faculty of Physics, Vilnius University, Sauletekio 9, LT-10222 Vilnius, Lithuania
[c] Instituto de Ciencia de Materiales de Sevilla (ICMS), CSIC – Universidad de Sevilla, c/ Américo Vespucio 49, 41092 Sevilla, Spain
[d] Institute of Low Temperature and Structure Research, Polish Academy of Sciences, ul. Okólna 2, 50-422 Wroclaw, Poland

ARTICLE INFO

Article history:
Received 29 November 2021
Received in revised form 20 January 2022
Accepted 24 January 2022
Available online 29 January 2022

Keywords:
YSZ
Sintering
Reducing atmosphere
CO_2+air atmosphereXPS
Electrical conductivity

ABSTRACTN

Given the need to process anodes and composites based on nano-YSZ in reducing or in air containing additional CO_2 atmospheres for the fabrication of solid oxide fuel cells (SOFCs), and solid oxide electrolysis cells (SOECs), we have studied the effect of the exposure to $CO+N_2/H_2$ or CO_2+air mixtures during sintering of YSZ green pellets, prepared from commercial nanopowders, on their structure, microstructure, chemical composition and their electrical properties. The reduced sample shows Raman bands at 1298 and 1605 cm^{-1} that are assigned to the D and G bands of carbon, respectively. The bands intensity ratio I_D/I_G indicates a larger content of disordered carbon. X-ray photoelectron spectroscopy (XPS) shows that C is present in the reduced samples as reduced carbon. However, the samples sintered in CO_2+air present C as carbonate-type. Impedance spectroscopy reveals that the highest total conductivity is for the reduced samples in the whole range of studied temperatures. In addition, sintering in CO_2+air causes a detrimental effect on the grain boundary conductivity and therefore, on the total electrical conductivity of YSZ. It can be due to the presence of impurities such as carbonates and oxidised or even, polymerised carbonaceous species located at those areas.

1. Introduction

Solid oxide fuel cells (SOFCs) are efficient and clean electrochemical devices that convert the chemical energy of a fuel into electricity. The electrolyte materials for SOFCs must be stable in reducing and oxidising environments and must have high ionic conductivity with low electronic conductivity at the cell operating temperatures. Until now, yttria-stabilized zirconia (YSZ) with a fluorite structure has been the most favoured electrolyte for SOFCs. In addition, porous Ni-YSZ composites are widely used as fuel electrodes [1–3]. Processing methods of anodes for fuel cells that use in situ carbon templating have been developed in order to generate a porous structure [4,5]. In this type of route, carbon usually surrounds the ceramic particles preventing them from sintering into larger particles and is burned away in air. Impurity phases such as monoclinic zirconia and ZrC can be formed during the process [5]. Despite those studies, the effect of related atmospheres generated when C templating is used during sintering of Ni-YSZ on the physicochemical characteristics of nano-zirconia has attracted until now little attention [6]. It should be analysed especially when both sintering and in situ reduction of anodes for SOFCs are implemented together in the fabrication of those devices [7].

YSZ is also used as one phase of dual ceramic composites in membrane reactors for natural gas conversion to syngas and for direct CO_2 electrolysis in SOECs [8–11]. These composites are used as dense ceramic membranes and present mixed oxygen ionic and electronic conductivities since they are constituted by YSZ and a perovskite with electronic conductivity. These composites are now attracting increasing attention [8–11] since with these latter membranes, chemical reactions such as partial oxidation of methane (POM), combustion of carbonaceous fuels and direct CO_2 electrolysis can be performed. For the preparation of those green membranes the tape casting technique involving phase inversion [10] and "tape casting-tape lamination-cosintering" are usually used and the employed slurries generally contain graphite [8–11]. Furthermore, in some cases hot-pressing is used for sintering those membranes. Then, air containing additional CO_2 will be the generated atmosphere during the thermal treatment of the tapes at high temperature [11]. Therefore, given then the need to process anodes or

* Corresponding author.
E-mail address: tcolomer@icv.csic.es (M.T. Colomer).

https://doi.org/10.1016/j.jallcom.2022.163976
0925-8388/

composites based on nano-YSZ in reducing or oxidising atmospheres containing CO or CO_2, respectively, we have studied the effect of the exposure to CO+N_2/H_2 or CO_2+air mixtures during sintering of nano-YSZ green pellets on their final structure, microstructure, chemical composition at the surface of the pellets, and their electrical properties. In addition, we have established the relationships among them. Furthermore, a previous characterisation of commercial powders used in the fabrication of SOFCs and SOECs is also mandatory in order to select the best sintering conditions to obtain the best microstructures and therefore, the best functional properties. Then, the characterisation of the commercial YSZ nanopowder used was also performed.

2. Experimental

2.1. Characterisation of YSZ nanopowders

The commercially available cubic ZrO_2 stabilized with 8 mol% Y_2O_3 nanocrystalline powders: 8YSZ from Nanostructured & Amorphous Materials Inc. (USA) was used as starting material. According to the supplier the mean particle size of the nanopowders is 51–65 nm with the following chemical analysis (wt%): Y_2O_3 (13.3), HfO_2 (2–3), Al_2O_3 (0.01), Fe_2O_3 (0.01), SiO_2 (0.02), and Na_2O (0.01). The specific surface area (S_{BET}) of the powders and density were measured in this study by one point N_2 adsorption (Monosorb, Quantachrome, USA) and He-multipicnometer (Quantachrome, USA), respectively. The errors of those techniques are ± 5% and ± 10%, respectively. The average particle size values (d_{BET}) were calculated from specific surface area measurements, assuming spherical, homogeneous primary particles, through the Eq. (1) [12].

$$d_{BET} = 6 / (S_{BET} \cdot \rho) \quad (1)$$

where S_{BET} is the measured specific surface, and ρ is the material density. Phase identification of the as-received powders was carried out by X-ray diffraction (XRD) with a diffractometer (X'Pert PRO, Panalytical, The Netherlands) using a Cu Kα radiation collected at room temperature over a range of $20° \le 2\theta \le 80°$ at a step scan rate of $2°s^{-1}$, with a step size of 0.02°. The results were processed using the ASTM-Files 37–1484, 01–083–0113, and 01–82–1246 for monoclinic, tetragonal and cubic phases, respectively. The crystal size was calculated using the Scherrer Eq. (2) [13]:

$$S = (K\lambda)/(\beta\cos\theta) \quad (2)$$

where K is the shape factor (0.9), λ is the X-ray wavelength (CuKα = 1.5418 Å), β is the full width at half maximum intensity (FWHM) in radians, and θ is the Bragg angle in degrees. The Rietveld refinement of the XRD patterns was performed using Jana2006 [14]. The background was fitted using Chebyschev polynomials; the peak profiles were fitted using a convolution of a pseudo-Voigt and asymmetry function. The crystal structure models of cubic [15], tetragonal [16] and monoclinic [17] phases were respectively taken from the references indicated. The volume fractions were calculated basing on the whole pattern fitting and the obtained values agreed well with a volume fraction calculated basing on separated high-angle diffraction peaks around 74°, using the method described in reference [18].

Raman spectra were recorded using a Renishaw InVia Raman spectrometer (Wotton-under-Edge, UK) equipped with a confocal DM2500 Leica optical microscope, a thermoelectrically cooled CCD as a detector, and a diode laser operating at 830 nm. The spectral resolution was 2 cm^{-1}. For the comparison, Raman spectrum was also recorded for the commercial powder using a green laser.

The microstructure of the commercial nanopowders was analysed by means of Field-emission scanning electron microscopy-energy dispersive x-ray (FEG-SEM-EDX) (Hitachi S-4700 type I, Tokyo, Japan). The powders were also characterized by transmission electron microscopy (TEM) using a JEOL JEM-2100 F microscope (Tokyo, Japan) operated at 200 keV accelerating voltage.

2.2. Sintering of powders

The nanopowders were compacted into disks by cold pressing, first uniaxially at 1 t and then isostatically at 200 MPa(CIP). In order to select the optimum temperature to obtain dense 8YSZ pellets, the apparent density of sintered samples was determined by the Archimedes method in water. Two different sintering atmospheres were employed: CO+N_2/H_2 (90 N_2:10 H_2 vol%) (reducing conditions) and CO_2+air. It was performed by burying always the green compact in a graphite powder bed and cushioned on a graphite plate under flowing atmosphere of 90 N_2/10 H_2 vol% (reducing conditions) or in air. Some naked pellets were also sintered in air for comparative purposes in some studies. The apparent density of the sintered samples was measured by Archimedes procedure in distilled water. The theoretical densities (ρ_{th}) were calculated applying the rules of mixing (Eq. 3) using the crystallographic densities mentioned below, and taking into account the cubic and tetragonal contents calculated by Rietveld refinement.

$$\rho_{th} = \nu_1\rho_1 + \nu_2\rho_2 \quad (3)$$

where ν_1 and ν_2 are the volume fractions of each phase calculated from XRD results, being ρ_1 and ρ_2 the crystallographic densities of cubic and tetragonal zirconia, respectively. Relative densities (% d_{th}) were calculated from experimental densities considering 100% the theoretical ones.

The crystallographic densities considered were for YSZ ρ_1 = 5.90 g cm^{-3} (ASTM 01–82–1246) and for YTZP ρ_2 = 6.10 g cm^{-3} (ASTM 01–083–0113).

Finally, 1350 °C for 2 h was selected as the best conditions for sintering (heating and cooling rate of 5 °C/min) since the highest densities were obtained at that temperature under both employed atmospheres (densities measured in the range of 1200–1350 °C).

2.3. Characterization of the sintered ceramics

Phase identification of the sintered samples was carried out by XRD with the equipment mentioned above and under the same conditions. The calculation of the lattice parameters and the volumes of the cells for the sintered samples was performed using a least-squares fitting method (Unitcell, Cambridge University, UK).

Phase identification of the sintered samples was also performed by Raman using the same equipment mentioned above and under the same conditions.

The microstructure of the sintered samples was observed by field emission scanning electron microscopy-energy dispersive X-ray (FEG-SEM-EDX) analyses (Hitachi S-4700 type I, Tokyo, Japan) on polished and thermally etched surfaces. Thermal etching at 1325 °C for 15 min in dry N_2 was employed. Average grain sizes of the microstructures were evaluated from the FESEM micrographs by an image processing and analysis program (ImageJ 1.53f51) that measures the surface of each grain and transforms its irregularly shaped area into a circle of equivalent diameter.

XPS measurements of the sintered samples were carried out in a PHOIBOS-100 spectrometer (SPECS Berlin, Germany) with a non-monochromatic Al Kα source ($h\nu$ = 1486.6 eV) being the power of the X-ray source 230 W (11.5 kV and 20 mA). The electron energy hemispherical analyser was operated in the constant pass energy mode (SPECS PHOIBOS 100DLD). Low resolution survey spectra were obtained with a pass energy equal to 50 eV, whereas high energy resolution spectra of the main photoemission peaks from the detected elements were obtained with 30 eV as pass energy. The

spectra were analysed with the "CASA XPS" software, version 2.3.16. Dev52 (Neal Fairly, UK). Shirley type backgrounds were used to determine the areas under the peaks.

Continuous wave (CW) electron paramagnetic resonance (EPR) measurements of the sintered samples at X-band microwave frequency (~9.7 GHz) were performed using a conventional Bruker ELEXSYS E580 EPR spectrometer (Karlsruhe, Germany) equipped with an ER4102ST rectangular cavity. For measurements, 2 mW microwave power was used. The strength and frequency of the modulation field were 4 G and 100 kHz, respectively.

Samples prepared as pellets of 0.8 cm diameter and 0.2 cm thickness were sputtered with Pt to serve as electrodes. Electrochemical impedance spectroscopy analyses (EIS) were performed in dry N_2 atmosphere between 300 and 900 °C. The impedance analyser used was a PGSTAT204 potentiostat/galvanostat (Metrohm Autolab, B.V., Switzerland) in the frequency range of 0.01–10^6 Hz. The impedance spectra were modelled in ZView®software using an equivalent circuit consisting of a series of resistances, R, in parallel with constant phase elements, CPE [19,20].

3. Results and discussion

3.1. Characterisation of the as-received commercial YSZ nanopowders

Rietveld refinement results of the as-received commercial nanopowder is shown in Fig. S1. It can be noted that the XRD pattern corresponds to cubic ZrO_2 phase as major phase and is highly crystalline (ASTM file 01–82–1246). The appearance of additional peaks corresponds to monoclinic zirconia (ASTM file 37–1484). According to Rietveld analysis the volume fraction of the cubic ZrO_2 is 0.73 and the volume fraction of monoclinic ZrO_2 is 0.27.

Raman spectrum of the commercial powder is presented in Fig. S2 (see Supplementary Information). It shows Raman bands at 631 + 613, 553, 472, 378, 342 + 328, 257, 188 and 176 cm^{-1}. These bands are characteristic for monoclinic phase [21]. The band at 613 cm^{-1}, visible as a shoulder, may also correspond to the cubic ZrO_2 which is in agreement with the XRD measurements.

The average crystal size (d_{XRD}) of the as-received powder calculated from the Scherrer's equation is 37 nm. The S_{BET} determined using the single point BET method and the density of the as-received powder are 18 ± 1 m^2g^{-1} and 5.69 $g{\cdot}cm^{-3}$, respectively. Microstructural observations made by FEG-SEM for the commercial powder (Fig. 1) show that the particles are agglomerated forming spherical granules of 100 µm, with the typical morphology of spray dried powders (Fig. 1a). At higher magnifications, nanoparticles of spherical shape and dimensions of approximately 50 nm can be distinguished (Fig. 1b). By TEM the average particle size observed is 30–40 nm (Fig. 2). Assuming monodispersed and spherical particles, an average diameter was calculated using the adsorption model from the nitrogen adsorption isotherm (d_{BET}) resulting in particles with an average size of 59 ± 2 nm. The BET approximation fits quite well SEM and TEM observations.

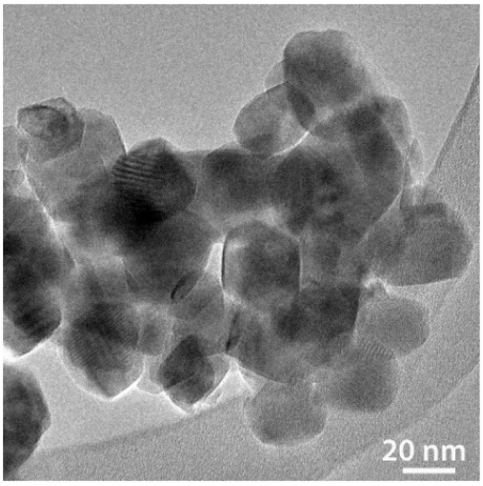

Fig. 2. Representative bright-field TEM image of as-received commercial YSZ nanopowders.

3.2. Characterisation of the sintered YSZ nanopowders

3.2.1. XRD

Figs. 3 and 4 show Rietveld refinement results of both the sample sintered under reducing conditions and the sample sintered in CO_2+air atmosphere, respectively. In a first estimation, the XRD patterns matched with the diffraction file of the cubic zirconia $Zr_{0.92}Y_{0.08}O_{1.96}$ (ASTM file 01-82–1246) as single phase. However, it can be observed that the peaks are not symmetrical showing shoulders that can be assigned to a zirconia tetragonal phase (YTZP) (ASTM file 01–083–0113). No peaks corresponding to monoclinic zirconia, ZrC or any other carbide are observed. According to Rietveld refinement results, the volume fraction of the cubic YSZ is 0.67 while the volume fraction of tetragonal YTZP is 0.33 for the reduced sample. For the sample sintered under CO_2+air the volume fractions are 0.70 for the cubic phase and 0.27 for the tetragonal one,

Furthermore, the peaks of the sample sintered under reducing conditions are slightly shifted to higher angles with respect to those of the sample sintered in CO_2+air. In turn, this observation indicates that the YSZ pellets sintered under reducing conditions have a

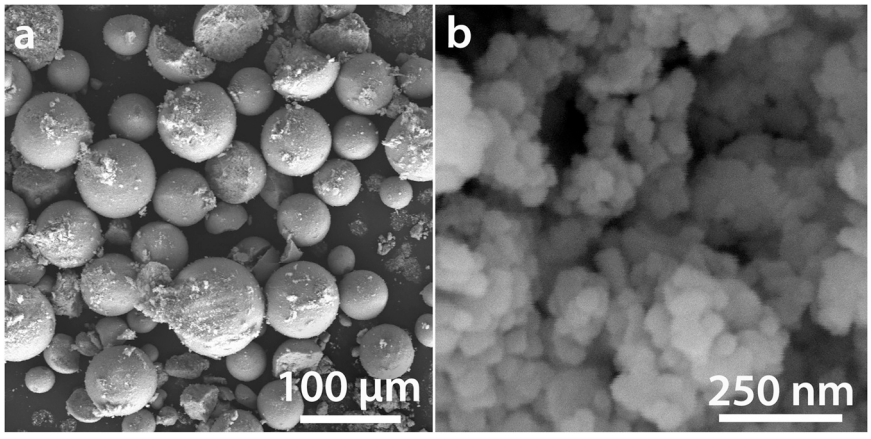

Fig. 1. Representative FEG-SEM images at different magnification of as-received commercial YSZ nanopowders.

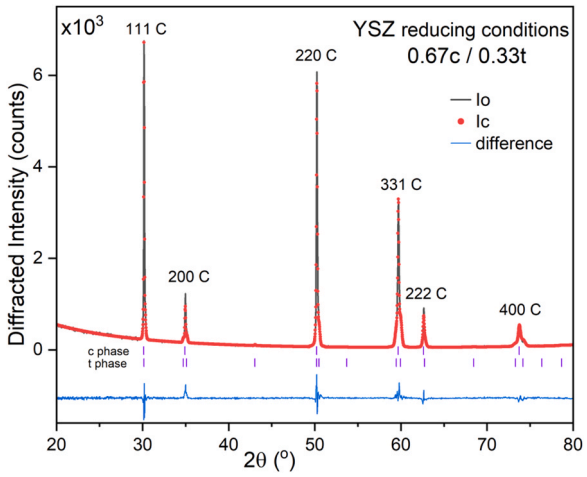

Fig. 3. XRD patterns and Rietveld refinement of the sintered YSZ pellets in reducing atmosphere ($CO+N_2/H_2$) consisting of cubic (c) and tetragonal (t) phases. Calculated (in red), experimental (in black) and difference intensities (in blue), positions of Bragg peaks (in purple). Rietveld discrepancy values [14]: Rp = 0.068; GOF = 1.35; R = 0.04 (for cubic structure); R = 0.056 (for tetragonal structure).

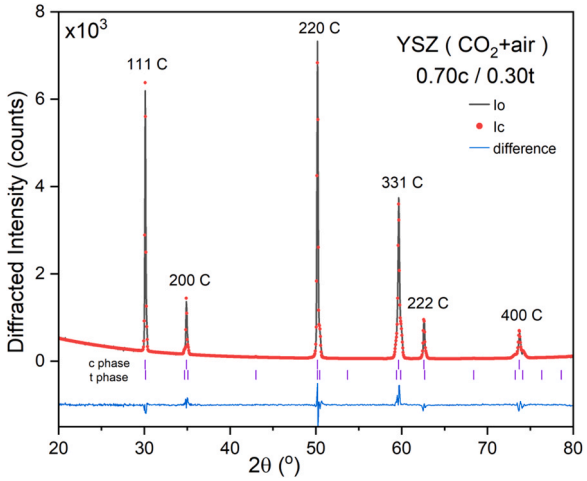

Fig. 4. XRD patterns and Rietveld refinement of the sintered YSZ pellets in CO_2+air consisting of cubic (c) and tetragonal (t) phases. Calculated (in red), experimental (in black) and difference intensities (in blue), positions of Bragg peaks (in purple). Rietveld discrepancy values [14]: Rp = 0.068; GOF= 1.35; R = 0.04 (for cubic structure); R = 0.056 (for tetragonal structure).

crystal structure with a smaller unit cell relative to that of the sintered in CO_2+air. This was further confirmed by the calculation of the lattice parameters and the volume of the cells. These calculations gave unit-cell volumes of 135.12 ± 0.01 and 135.38 ± 0.07 Å^3 for samples sintered under $CO+N_2/H_2$ and CO_2+air, respectively. It could indicate a larger concentration of oxygen vacancies when the sample is sintered under reducing conditions. Both volumes are smaller than that of obtained by Yashima et al. [22] for YSZ sintered in air (136.37 Å^3). The volume decrease, if we compare our results with that by Yashima et al. [22], is in accordance with the previous study by Akgenc and Cagin [23] that observed a linear decrease in the YSZ cell volume when oxygen vacancies increase due to the increasing dopant concentration (Y_2O_3 in that case). In this study, the increase in oxygen vacancies can be due to the incorporation of C and/or N in the YSZ lattice as it was observed in previous works [24–27]. Xiang et al. [24] observed the formation of a solid solution of carbon atoms in the tetragonal zirconia lattice exhibiting a significant oxygen

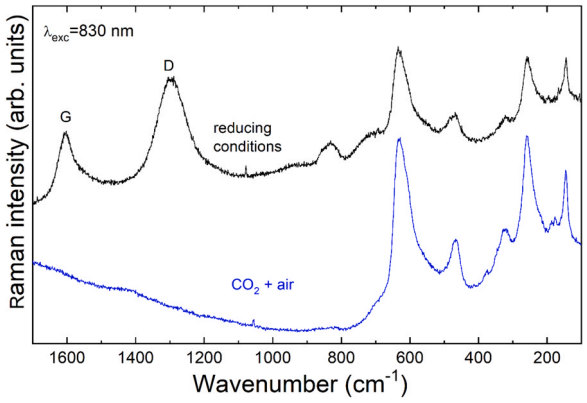

Fig. 5. Raman spectra of the samples sintered under reducing ($CO+N_2/H_2$) conditions and in CO_2+ air atmosphere.

deficiency. If carbon atoms enter into the lattices of zirconia and substituted the oxygen atom, the oxygen vacancies can be produced by the following reaction (Eq. 4) [25].

$$C \xrightarrow{ZrO_2} C''o + V\ddot{o} \quad (4)$$

where C˝o represents a C anion replacing an oxygen anion in the lattice.

In addition, Luo et al. [26] observed the decrease of the interplanar distances by TEM for all the peak-positions of a cubic zirconia as a result of the entrance of carbon into the lattice of ZrO_2. In nitrogen doped zirconia oxygen vacancies are created according to the following (Eq. 5) [27]:

$$N_2\,(gas) + 3Oo \leftrightarrow 2\,N'_O + V_{\ddot{o}} + 3/2\,O_2\,(gas) \quad (5)$$

where N'_O represents a nitrogen anion replacing an oxygen anion in the lattice.

Finally, the relative densities of the samples after sintering were ~ 99.97% and 99.94% ρ_{th} for the samples sintered in reducing conditions and CO_2+air, respectively.

3.2.2. Raman spectra

Raman spectra of the sintered samples are presented in Fig. 5. The sample sintered in reducing conditions shows bands at 632, 467, 323, 259, and 144 cm^{-1} that can be attributed to tetragonal ZrO_2 [28]. There is also a band near 610 cm^{-1} visible as a shoulder that corresponds to the cubic ZrO_2. Thus, this sample contains both tetragonal and cubic phase. This conclusion is also supported by the fact that the Raman spectrum is very similar to that reported for mixtures of ZrO_2 doped with 3 and 8 mol% Y_2O_3, which contained both cubic and tetragonal phases [29]. It is worth noting that the Raman spectrum also shows a band at 706 cm^{-1}. This band points to presence of a small amount of $Y_2Zr_2O_7$ pyrochlore [30,31]. The formation of the pyrochlore phase can be explained due to the extremely low Gibbs free energy formation: − 4593 kJ/mol at 1000 °C and − 4918 kJ/mol at 1500 °C, using the function given by Schaedler et al. [32] In addition, the black sample also shows two intense bands at 1605 and 1298 cm^{-1} that correspond to the G and D bands of carbon, respectively [33]. The position of the G band is in good agreement with literature data reported for leaf char (1598 cm^{-1}) [33] or activated carbon prepared from carbon black or cokes (1598–1614 cm^{-1}) [34]. However, the D band of our sample is observed at a significantly lower wavenumber value (1298 cm^{-1}) than the D band of leaf char (1340 cm^{-1}) [33] or activated carbon (1343–1363 cm^{-1}) [34]. This effect can be attributed to the application of different laser lines, i.e., near-IR laser line in our case (830 nm) and visible laser line (514.5 nm) in the mentioned above literature spectra. Indeed, former studies of carbon materials showed that the position of the G band

weakly depends on the laser excitation wavelength whereas D band exhibits a large shift to lower wavenumber with increasing excitation wavelength [35]. It is well-known that D band corresponds to disordered carbon (amorphous C), while G band represents the in-plane bond-stretching motion of the pairs of C sp^2 atoms of graphite, representing an ordered structure [33–35]. The band intensity ratio of the D and G band is often used as a useful parameter expressing the relative content of the disordered to ordered carbon [34,35]. In our case the I_D/I_G value is large (3.8), indicating a larger content of the disordered carbon. According to previous studies in YTZP samples sintered in Ar and prepared from Zr (IV) acetylacetonate carbon atoms enter into the zirconia lattice and act as stabilizer [24]. The amorphous carbon creates a reducing atmosphere, meanwhile carbon atoms bonded with zirconium atoms act as a stabilizer.

The additional bands observed near 730 and 850 cm^{-1} in the reduced YSZ sample are most likely related to defect-induced vibrational modes [36]. Such additional bands appear if there are some defects and/or disorder. It may be interpreted as disorder/defect-induced vibrational modes, normally symmetry-forbidden, which can become Raman active through a loss of symmetry because of a breakdown in the selection rules. In addition, the observation of this broad signal should reflect a strong disorder within the O sublattice, due to oxygen vacancies ($V_{ö}$). In our case, we may have instead of ZrO_6 octahedral units in the structure, also some ZrO_5 units due to vacancies. In such case, Zr-O bond would be shorter and therefore Raman band should be observed at a higher wavenumber value. The sample sintered in CO_2+air shows the same Raman bands characteristic for the cubic and tetragonal ZrO_2 as well as $Y_2Zr_2O_7$ pyrochlore. In addition, a weak band near 1055 cm^{-1} could probably be attributed to a carbonate [37]. However, the intensity of this peak indicates that the amount should be very small.

3.2.3. FEG-SEM-EDX

Typical microstructures of the YSZ material sintered under CO +N_2/H_2 atmosphere and in CO_2+air at 1350ºC for 2 h, after polishing and thermal etching, are shown in Fig. 6a and b, respectively. The pictures show fully densified bodies were obtained after sintering. Fig. 7a and b show the dependence of the grain size distribution for the sintered samples. Around 84–85% of grains have an average grain size lower than 0.56 µm, and around 14% of grains have an average grain size lower than 1.26 µm in both samples. Finally, only 0.7% have an average grain size of 1.78–1.87 µm in the reduced samples and 0.4% of 1.69–1.78 µm in the samples sintered under CO_2+air atmosphere, respectively.

EDX semi-quantitative analyses of the larger grains (0.98–1.87 µm) for the samples sintered under reducing conditions gave ≈ 65.0–66.1 wt% ZrO_2, 7.1–8.6 wt% Y_2O_3, and 0.9–1.5 wt% Hf_2O_3. They can be identified as YSZ. Meanwhile the analyses gave ≈ 67.8–68.1 wt% ZrO_2, 5.9–6.1 wt% Y_2O_3, 0.5–0.6 wt% Hf_2O_3, values for the finer grains that could correspond to YTZP (sizes lower than 0.98 µm). EDX semi-quantitative analyses of those samples gave ≈ 65.5–65.7 wt% ZrO_2, and 8.9–9.1 wt% Y_2O_3 values for the large grains (from 0.98 to 1.78 µm) that can be then identified as YSZ. Meanwhile the analyses gave ≈ 66.6–67.2 wt% ZrO_2, 6.1–7.3 wt% Y_2O_3, and 0.7–1.3 wt% Hf_2O_3 values for the finer grains (sizes lower than 0.98 µm) that could correspond to YTZP. In the larger grains of the cubic zirconia, Hf_2O_3 is not detected.

Based on our XRD, Raman and FEG-SEM-EDX results, we can consider the samples as YSZ-YTZP composites. $Y_2Zr_2O_7$ pyrochlore phase was not detected by means of FEG-SEM-EDX analyses. It can be due to the well-known fact that this phase is generally observed at the surface of the cubic grains [30,31,38] and if the amount is small the polishing of the samples can remove it.

3.2.4. XPS

In order to investigate the nature of the surface of the materials and its chemical composition, XPS spectra were analysed for sintered samples under CO+N_2/H_2 (reducing conditions), CO_2+air, and air atmospheres. The latter was also studied for comparative purposes. Fig S3 shows the survey spectra of the three samples studied. Due to the insulating nature of these materials at room temperature, binding energy (BE) correction had to be performed. It has been observed that the addition of yttria to zirconia causes a shift in the Zr 3d and O 1 s photoemission peaks. In addition, the first two types of samples have shown numerous peaks in the C 1 s signal that make the use of these signals as typical calibration difficult. For these reasons, it was preferred to cancel the charging effects by calibrating of all the spectra with Y 3d signal to 158.9 eV [39]. Y 3d peak does not shift for an increasing yttria content and only leads to an increment of the signal intensity.

The integration of the area beneath the peaks allows us to calculate the relative concentrations of all the elements for each sample. These quantifications are evaluated as relative concentration in atomic concentration (at%). The results are shown in Table 1.

In all cases, the presence of small amounts of Na and Si impurities from the as-received commercial nanopowder used has been detected. Interestingly, there is not any signal of Fe or Al on the surface of the pellets, although the corresponding chemical analyses

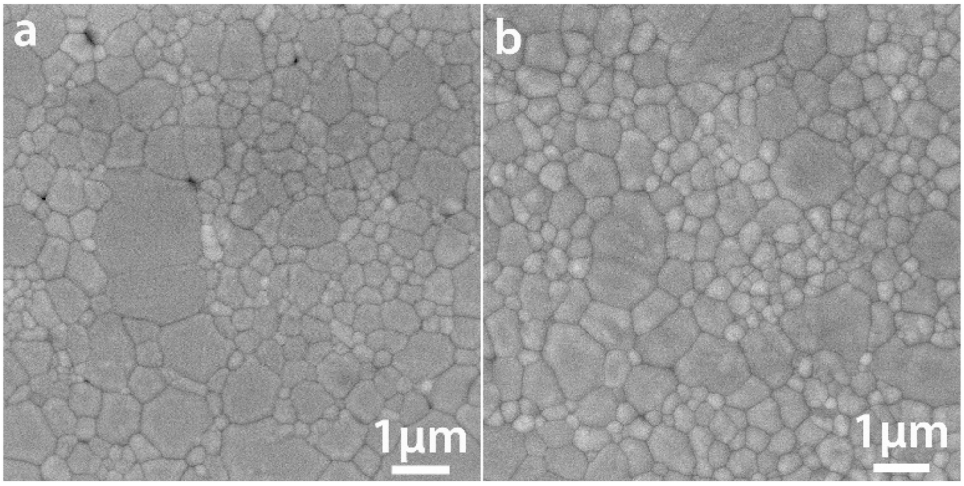

Fig. 6. Representative FEG-SEM micrographs of polished and thermal etched surfaces under dry N_2 of the sample sintered under reducing conditions (CO+N_2/H_2) (a) and at the same conditions but for the sample sintered under CO_2+air atmosphere (b).

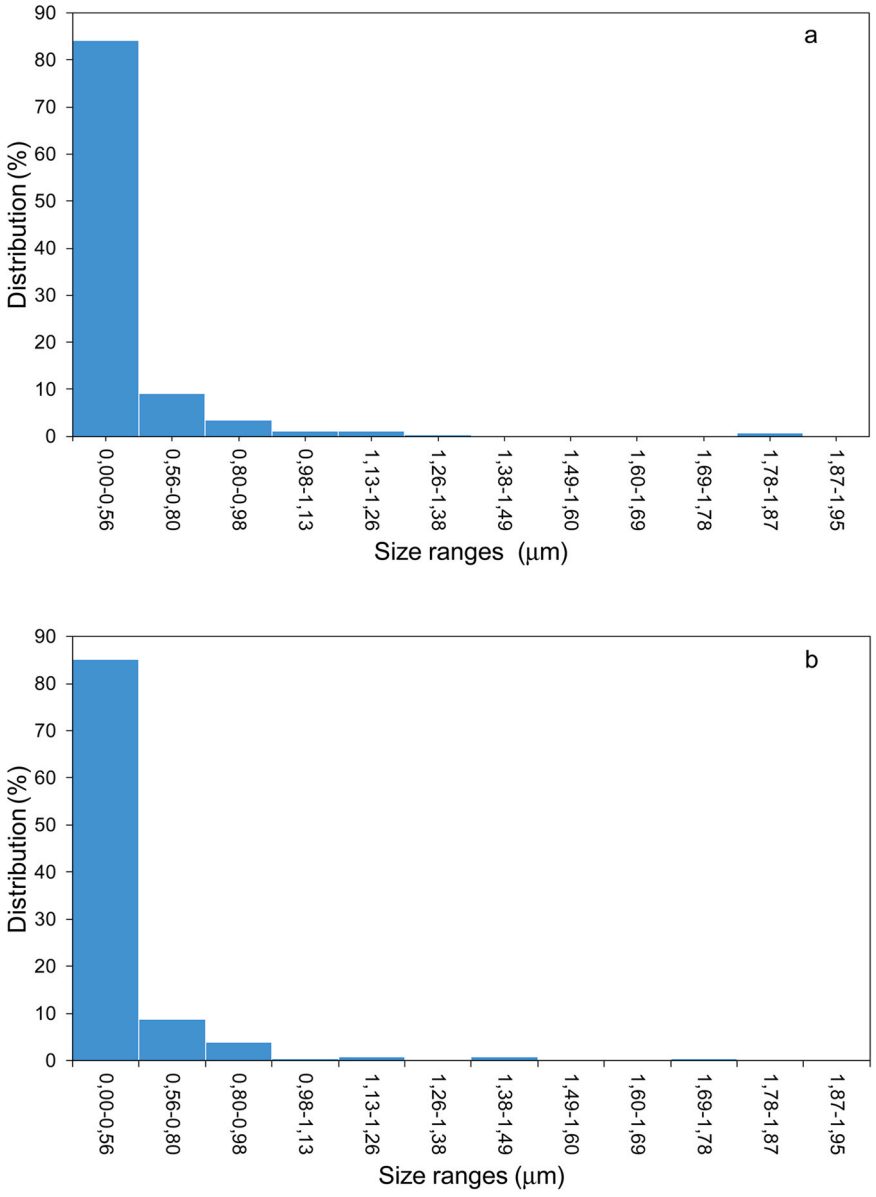

Fig. 7. Grain size distribution of the samples sintered under reducing conditions (a) and sintered under CO_2+air atmosphere (b).

of the supplier show that these elements are also present as impurities. High resolution spectra of the major elements are shown in Fig. S3. The Zr 3d photoemission signal consists of a doublet at BE 186.1 and 183.7 eV corresponding to $3d_{3/2}$ and $3d_{5/2}$ peaks, respectively. These values are slightly higher than those reported for zirconia [39–41] according to the shift caused by the incorporation of yttria, as it is mentioned above. The pellets prepared under reducing conditions (a) and under CO_2+air (b) show a broad BE asymmetric signal of the O 1 s peak at 532.0, and 532.5 eV, respectively, indicating two types of oxygen coordination. However, the samples sintered in air (c) show a symmetrical O 1 s signal constituted by only one sharp and narrow peak at 531.6 eV. It could indicate only one type of O coordination at the surface of these latter samples. Since the value of BE is lower than those of the samples sintered under reducing conditions and under CO_2+air, the absence of OH groups and/or coordinated water at the surface for the sample sintered in air is plausible.

The Y $3d_{5/2}$ peak appears at a BE of 158.9 eV in all cases and it has been used as a calibration reference, as it is mentioned above [40]. Moreover, the Y/Zr atomic ratio obtained from the XPS analyses for the studied samples is within the range of the Y/Zr theoretical ratio calculated for YSZ, Y/Zr = 0.17-0.18 (Table 1), corroborating that the pellets present cubic phase as major phase, in agreement with the XRD analyses.

In the samples prepared under reducing conditions the N 1 s peak is detected at 400.9 eV (not shown here for the sake of brevity)

Table 1
Elemental composition in at% of the surface for the YSZ samples sintered under reducing conditions ($CO+N_2/H_2$), CO_2+air, and air.

Sample	Na (at%)	O (at%)	Zr (at%)	C (at%)	Y (at%)	Si (at%)	N (at%)	Y/Zr
$CO+N_2/H_2$	1.4	37.1	11.7	43.6	2.2	3.3	0.7	0.18
CO_2+air	1.2	39.5	12.5	41.6	2.2	2.9	–	0.17
Air	1.8	54.5	18.0	19.9	3.1	2.6	–	0.17

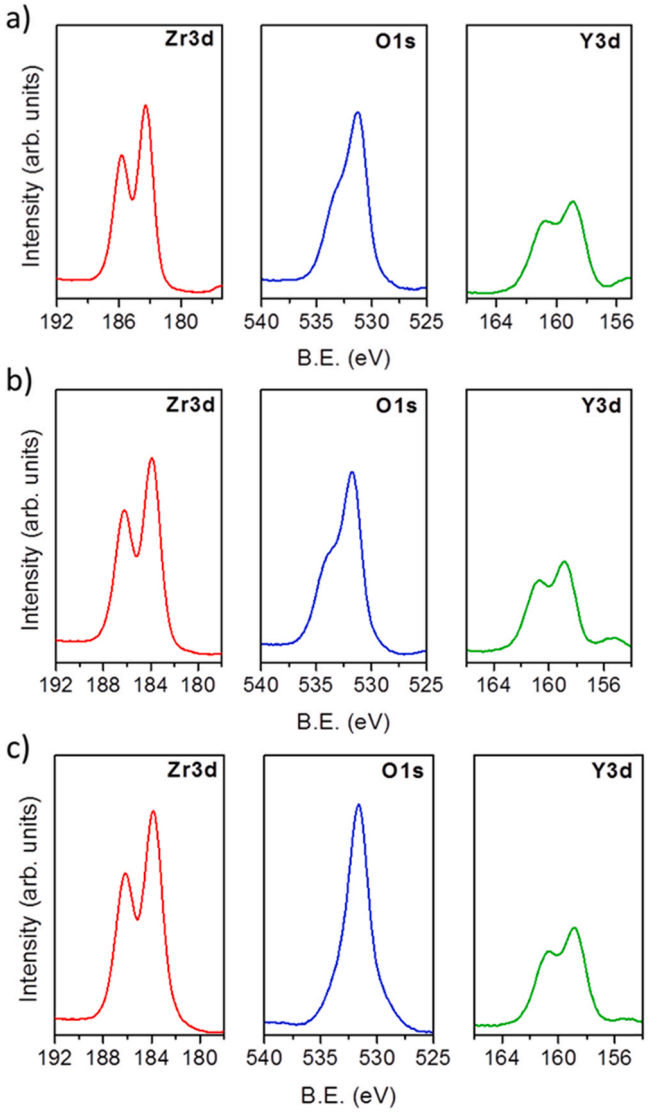

Fig. 8. High resolution spectra for Zr 3d, O 1s and Y 3d photoemission signals of the YSZ sintered under reducing conditions (a), under CO_2+air (b), and in air (c).

with a very low intensity (0.7 at%). The BE value is in accordance with an oxynitride coordination in nitrogen-doped YSZ, as it is reported in the literature [39,40]. In contrast, the samples sintered under CO_2+air and in air atmospheres do not show any nitrogen signal, as it is expected. Fig. 8.

Additional information can be obtained from the carbon C 1 s photoemission spectra (see Fig. 9). For the samples sintered under reducing conditions the C 1 s peak appears at 281.4 eV which is in accordance with a reduced carbon, even carbide. The presence of this type of C can be caused by the sintering conditions [42]. For the samples sintered in CO_2+air the C 1 s photoemission signal has a peak at 286.4 eV, a value that corresponds to a carbonate-type carbon [43]. In addition, a shoulder at a higher BE value, 209 eV, that could belong to more oxidised species, or even polymerised, with > C=O and C(=O)O bonds [43c-d], is detected. This contribution, around 8% of the total carbon at the surface of the sample, can be due to the residual organic product added to the commercial nanopowder during its processing. Then, 92% of the remaining carbon would correspond to a carbonate. Finally, the photoemission signal from C 1 s of the sample sintered in air shows two well-defined peaks at BE of 286.4 and 283.5 eV. The highest value corresponds to a carbonate-type carbon [42], as it is mentioned above, and the lowest

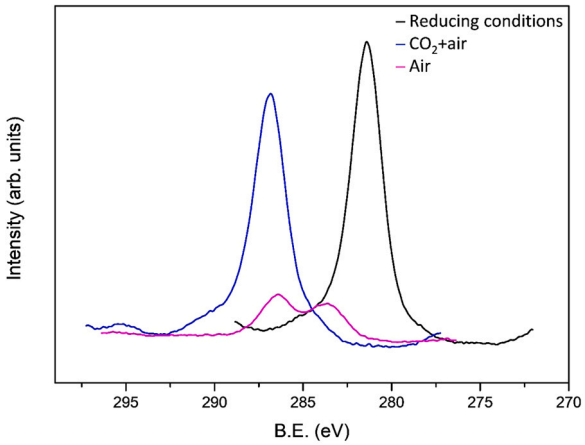

Fig. 9. XPS spectra of C 1 s photoemission peak for YSZ samples sintered in reducing conditions (a), under CO_2+air (b), and in air (c).

BE peak can be attributed to adventitious carbon coming from the environment. As it is expected, the sample sintered in air has a much lower carbon content (Table 1).

3.2.5. EPR

The CW X-band EPR spectra were recorded for all samples at room temperature and at − 173 °C. No significant changes in the spectra occurred while cooling the samples. The results obtained at room temperature are presented in Fig. 10. No EPR signal was resolved for the sample sintered under CO+N_2/H_2 atmosphere. In contrast, the sample sintered under the same atmosphere but later treated in air under 900 °C exhibits a strong signal in the low-field region with the *g*-factor value of about 4.3. It is well-known that such a signal originates from Fe^{3+} ions in the high electron spin (S = 5/2) state [44]. To trace the origin of the iron, we measured raw ZrO_2 powder which was used to prepare the samples and indeed the same EPR signal was observed (not shown here for the sake of brevity). However, the sample sintered under CO+N_2/H_2 atmosphere does not show this signal. It can be due to a probable reduction of the Fe^{3+} impurities to EPR silent Fe^{2+} [45]. In addition to this iron signal, the sample sintered under CO_2+air shows an asymmetrical signal at g = 1.97. A very similar signal was observed in electron and ion-irradiated YSZ. It was assigned to F^+-type centres involving singly-

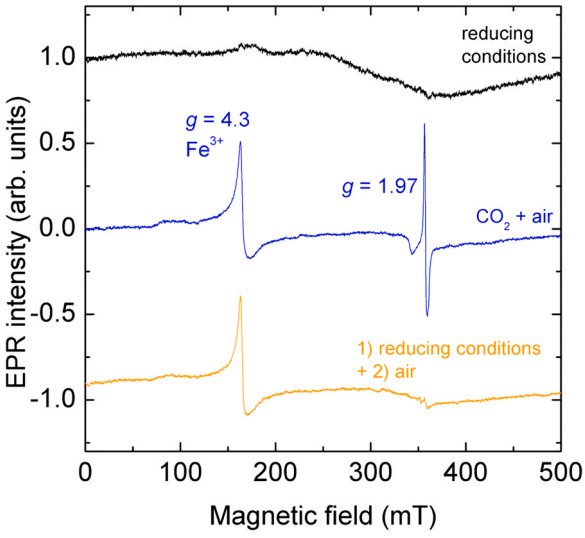

Fig. 10. EPR spectra of the pellets sintered under reducing conditions, under CO_2+air and oxidised after reducing conditions, i.e., 1) reducing conditions + 2) air.

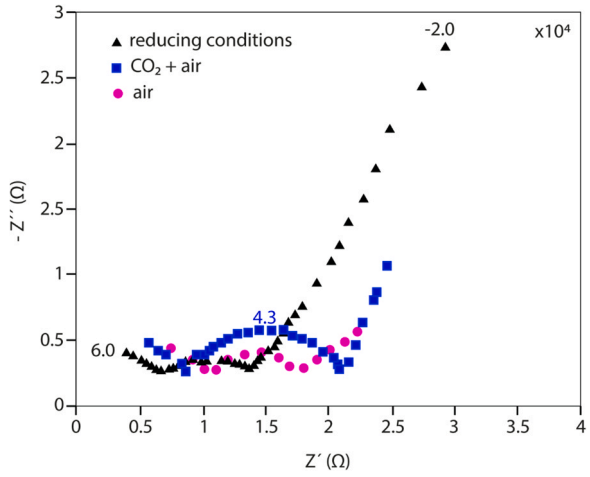

Fig. 11. Representative impedance spectra obtained at 400ºC in dry N_2 for the different samples studied. The impedance spectrum of a pellet sintered in air is also depicted for comparative purposes. Numbers on the arcs are the logarithm of the frequency in Hz.

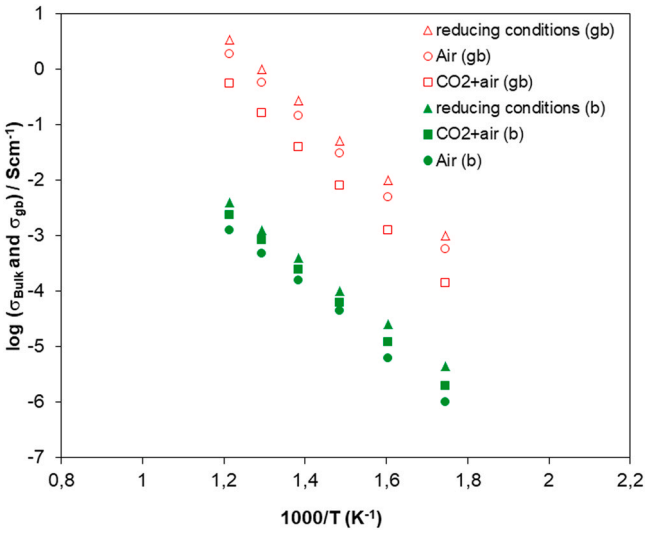

Fig. 12. Arrhenius plots of the bulk (b) and grain boundary (gb) conductivities of the sintered samples as a function of the inverse of temperature in the range of 300–600 °C in dry N_2.

ionized oxygen vacancy Vȯ [46,47]. Note that we did not detect any EPR signal of Zr^{3+} divacancies (T-centers) which is frequently observed in YSZ [48,49].

3.2.6. AC electrical measurements: impedance spectroscopy measurements in dry N_2

Fig. 11 shows representative impedance spectra of the samples sintered under reducing conditions and under CO_2+air atmosphere at 400ºC measured in dry N_2. The impedance spectrum of a pellet sintered in air is also shown for comparative purposes. The impedance spectra of the three samples display three features at high (HF), medium (MF), and low frequencies (LF), characteristic of oxygen ion conductors [50,51]. The high frequency arcs (only a part is observed) are ascribed to the YSZ bulk (lattice) meanwhile the medium frequency corresponds to the grain boundaries and the spike line at low frequencies is a distributive dispersion effect associated with a general diffusion related equivalent circuit element, namely a constant phase element (CPE), respectively. Here, the observed CPE distributive effect is physically interpreted as produced by both, a grain boundary blocking effect and the interface between the Pt-electrode and the sintered pellet. In all samples, the electrical behavior is clearly dominated by the oxygen-ion conductivity, as evidenced by the capacitive responses of the bulk and grain boundaries observed in the corresponding impedance spectra (Fig. 11) and for the activation energies (see below). The sample sintered in reducing conditions (black on the chart) has the smallest grain interior impedance. This may be due to a larger concentration of $V_{ö}$ in the lattice that involves a greater bulk conductivity. The increased oxygen vacancies content can be due to the formation of solid solutions in which C and/or N could enter into the ZrO_2 lattice, as it was discussed above. In particular, the O and C contents of the reduced sample are the lowest and the highest, respectively, if it is compared with the rest of the studied samples. In addition, N is only present in the sample treated under reducing conditions, as it is expected. The sample sintered under CO_2+air atmosphere presents higher bulk conductivity if it is compared with the sample sintered in air. It can be also related with the formation of a solid solution of carbon atoms in the zirconia lattices generating $V_{ö}$ but in a lower concentration than that of the sample sintered under reducing conditions. It agrees well with the oxygen content quantified by XPS in these latter samples.

The bulk conductivity is an intrinsic property of the material, and, therefore, it is independent of the microstructural features of a polycrystalline material. However, small differences can be expected when a second phase is blocking the charge carriers. These differences are observed at frequency ranges associated with grain boundary interfaces, when impedance is measured at low temperatures. It is well-known that the grain boundary microstructure is easily influenced by the nature and amount of impurities, the sintering conditions and cooling rates. In this study, we observed a flattened shape of the grain boundary arcs that could be due to the presence of residual carbonaceous species that block the oxygen vacancies transport. The largest grain boundary impedance is detected for the sample sintered in CO_2+air. It can be associated with a higher amount of impurities such as oxidised or even, polymerised carbonaceous species and a carbonate located at those areas.

As the cubic phase is predominant in the samples it is the main one responsible for conduction according to the brick layer model and percolation theory [51,52]. In composite yttria-substituted zirconia solid electrolytes containing cubic and tetragonal phases, the percolation threshold of cubic phase is located at 70 vol% of cubic phase [53]. In our samples and according to Riteveld refinements the vol% of cubic phase is 67% and 70% for the samples sintered under reducing and CO_2+air atmospheres, respectively. Then, we can assume that the cubic phase is percolated and it is the main one responsible for conduction. Fig. 12 shows the bulk and grain boundary conductivities of the samples as a function of the inverse of the temperature in the range of 300–600ºC. A linear behaviour is found in both conductivities for the three samples.

Fig. 13 shows the Arrhenius plots of the total conductivity of the sintered samples as a function of the inverse of the temperature in the range of 300–900ºC in dry N_2. As can be seen, a linear behavior is found for the three samples at low temperature (up to 700ºC) and the usual bending toward lower activation energies was found in all cases at higher temperatures (from 700ºC). This fact is well-known and can be due to the breakdown of the defect association $(Y'Zr\text{-}V_{ö})^{\cdot}$ with vacancy trapping and resulting mobile oxygen vacancies [54,55]. Though the total conductivity results obtained for the studied samples are similar at the lowest temperature the difference increases with increasing temperatures. This is mainly due to differences in activation energy of the bulk conductivity (1.05 ± 0.01, 1.11 ± 0.01 and 1.12 ± 0.01 eV for the samples sintered under reducing conditions, under CO_2+air, and in air, respectively).

The values of the total ionic conductivity of YSZ sintered under reducing conditions are higher compared with those sintered in air

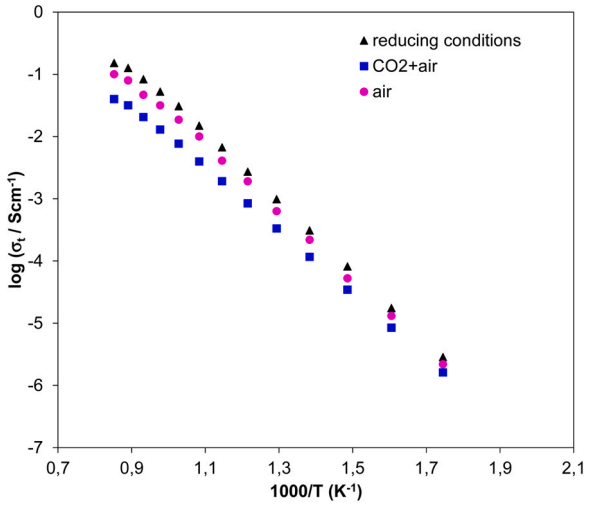

Fig. 13. Arrhenius plots of the total conductivity of the sintered samples as a function of temperature in the range of 300–900 °C in dry N_2.

and under CO_2+air. In addition, the activation energy is indicative of the nature of the charge carrier and conduction mechanism. In the high temperature range (700–900ºC), the activation energy of the total conductivity is 0.92 ± 0.01, 0.93 ± 0.01, and 0.94 ± 0.01 eV for the samples sintered under reducing conditions, under CO_2+air, and in air, respectively. The conductivity values of YSZ treated under reducing conditions are larger when they are compared with previous values obtained for YSZ sintered and measured under reducing conditions (Ar-4% H_2). However, the conductivity values obtained for YSZ treated under CO_2+air are lower than that of YSZ sintered in air in this study and in a previous one where YSZ was measured under reducing conditions (Ar-4% H_2) [56]. These findings are in accordance with the study of Tailor et al. [57] that investigated the effect of nitrogen and carbon impurities in ZrO_2 on the electrical properties using the density functional theory with a hybrid functional method. That method allows more accurate predictions of formation energies and defect levels, by comprehensively addressing all possible atomic configurations and charge states. Those authors found that nitrogen is present in positive charge states, being the dominant defects N'_O and $V_{\ddot{O}}$. This picture is consistent with the Kröger-Vink reactions mentioned above where the substitution of C and/or N into the lattice creates $V_{\ddot{O}}$. In addition, they found that carbon impurities have relatively low formation energies and would indeed incorporate easily during growth of ZrO_2, but those impurities do not affect the equilibrium between nitrogen and oxygen vacancies. Finally, in a previous study, the intentional doping of N in YSZ films has been shown to lead to an increased ionic conductivity at high temperatures [58]. Those findings are in accordance with the fact that the highest total conductivity values found in this study are for the sample treated under reducing conditions. Furthermore, the presence of CO_2 during sintering seems to be detrimental for the grain boundary conductivity and therefore, for the total conductivity of YSZ (Figs. 11–13). It can be associated with the presence of impurities such as carbonates and residual oxidised or even polymerised carbonaceous species found by XPS analysis.

4. Conclusions

Based on the experimental results and analyses, the following conclusions can be drawn:

Dense pellets of YSZ have been obtained after sintering at 1350ºC for 2 h in reducing atmosphere ($CO+N_2/H_2$) or in CO_2+air from commercial nanopowders. Raman spectra and XRD patterns indicate that both samples are constituted not only by cubic (major phase) but also by tetragonal zirconia. In addition, $Y_2Zr_2O_7$ pyrochlore is present as a minor phase. Furthermore, the sample sintered under reducing conditions shows bands at 1298 and 1605 cm^{-1} that correspond to the D and G bands of carbon, respectively. The band intensity ratio of the D and G band, I_D/I_G, value is 3.8 indicating a larger content of disordered carbon. XPS showed that the samples sintered under reducing conditions contain N and C being the latter element present as reduced C, even as a carbide. However, C as carbonate-type is present in the samples sintered under CO_2+air atmosphere. Impedance spectroscopy reveals that the lowest grain interior impedance corresponds to the samples sintered under reducing conditions. In addition, that sample presents the highest total conductivity in the whole range of temperatures studied that can be associated to a larger number of oxygen vacancies, in accordance with the presence of N and C and the lowest oxygen content in that sample, as was determined by XPS. Furthermore, the presence of CO_2 during sintering seems to be detrimental for the electrical properties of YSZ.

CRediT authorship contribution statement

M.T. Colomer: Conceptualization, Writing – review & editing, Resources, Investigation, Methodology, Funding acquisition. **M. Simenas:** Investigation, Writing. **J. Banys:** Investigation. **F. Vattier:** Investigation, Writing. **A. Gagor:** Investigation, Writing. **M. Maczka:** Investigation, Writing.

Declaration of Competing Interest

The authors declare that they have no known competing financial interests or personal relationships that could have appeared to influence the work reported in this paper.

Acknowledgments

This work was partially supported by the Science and Innovation Ministry (Government of Spain) and cofinanced with FEDER Funds under the Grant PID2019-104118RB-C21. The authors acknowledge to Dr. D.G. Calatayud for his help in the analysis of the distributions of the average of grain sizes for the sintered samples. In addition, the authors are also grateful to Mrs. C. Díaz-Dorado for her help in the preparation of FEG-SEM and TEM figures. We also acknowledge support of the publication fee by the CSIC Open Access Publication Support Initiative through its Unit of Information Resources for Research (URICI).

Appendix A. Supporting information

Supplementary data associated with this article can be found in the online version at doi:10.1016/j.jallcom.2022.163976.

References

[1] A. McEvoy, High temperature solid oxide fuel cells: Fundamentals,design and applications, in: S.C. Singhal, K. Kendall (Eds.), Fuel Cells: Fundamentals, Design and Applications, Elsevier, 2003(Chapter 6).
[2] A. Atkinson, S. Barnett, R.J. Gorte, J.T.S. Irvine, A.J. McEvoy, M. Mogensen, S.C. Singhal, J. Vohs, Advanced anodes for high-temperature fuel cells, Nat. Mater. 3 (2004) 17–27.
[3] W.Z. Zhu, S.C. Deevi, A review of the status of anode materials for solid oxide fuel cells, Mater. Sci. Eng. A362 (2003) 228–239.
[4] M.T. Colomer, E. Nieto, J.R. Jurado, Developing a thick-film cermet, Am. Ceram. Soc. Bull. 75 (9) (1996) 85–88.
[5] S.P. Muhoza, A. McCormack, R.W. Garrett, M.D. Yuce, V.S. Prathab, S.K. Hambright, M.A. Cottam, M.D. Gross, Processing nano-YSZ in solid oxide fuel cells: the effect of sintering atmosphere on thermochemically stability, J. Electrochem. Soc. 166 (2019) F53–F58.
[6] C.-J. Ho, W.-H. Tuan, Phase stability and microstructure evolution of yttria-stabilized zirconia during firing in a reducing atmosphere, Ceram. Int. 37 (2011) 1401–1407.

[7] Z. Han, Z. Yang, M. Han, Fabrication of metal-supported tubular solid oxide fuel cell by phase-inversion method and in situ reduction, Int. J. Hydrog. 41 (2016) 10935–10941.

[8] T. Liu, Y. Wang, R. Yuan, J. Gao, C. Chen, H.J.M. Bouwmeester, Enhancing the oxygen permeation rate of $Zr_{0.84}Y_{0.16}O_{1.92}$–$La_{0.8}Sr_{0.2}Cr_{0.5}Fe_{0.5}O_{3-\delta}$ dual-phase hollow fiber membraneby coating with $Ce_{0.8}Sm_{0.2}O_{1.9}$ nanoparticles, ACS Appl. Mater. Interfaces 5 (2013) 9454–9460.

[9] Y. Zhang, R.-H. Yang, J.-F. Gao, C.-S. Chen, Oxygen permeation properties of supported planar $Zr_{0.84}Y_{0.16}O_{1.92}$–$La_{0.8}Sr_{0.2}Cr_{0.5}Fe_{0.5}O_{3-d}$ composite membranes, Sep. Purif. Technol. 166 (2016) 142–147.

[10] C. Li, X. Ban, C. Chen, Z. Zhana, Sandwich-like symmetric dual-phase composite membrane with an ultrathin oxygen separation layer and excellent durability, Solid State Ion. 345 (2020) 115176.

[11] C. Cui, Y. Wang, Y. Tong, Z. Zhan, C. Chen, S. Wang, Direct CO_2 electrolysis on symmetric $La_{0.8}Sr_{0.2}Cr_{0.5}Fe_{0.5}O_{3-\delta}$-$Zr_{0.84}Y_{0.16}O_{2-\delta}$ electrode-supported solid oxide electrolysis cells, J. Electrochem. Soc. 168 (2021) 024508.

[12] S.J. Gregg, K.S. Sing, Surface Area and Porosity, Academic Press, London, UK, 1992.

[13] A.L. Patterson, The Scherrer formula for x-ray particle size determination, Phys. Rev. 56 (10) (1939) 978–982.

[14] V. Petricek, M. Dusek, L. Palatinus, Crystallographic computing system Jana2006: General features, Z. Krist. 229 (5) (2014) 345–352.

[15] D.-N. Wang, et al., Science in China, series a: mathematics, physics, Astronomy 42 (1999) 80.

[16] G. Teufer, The crystal structure of tetragonal ZrO_2 ICSD 23928, Acta Cryst. 15 (1962) 1187-1187.

[17] D.K. jr Smith, H.W. Newkirk, Crystal structure of zirconia by rietveld refinement, Acta Crystallogr. 18 (1965) 983–991.

[18] A. Paterson, R. Stevens, Phase analysis of sintered yttria-zirconia ceramics by x-ray diffraction, J. Mat. Res. 1 (1986) 295–299.

[19] D.Y. Wang, A.S. Nowick, The grain boundary effect in doped ceria solid electrolytes, J. Solid State Chem. 35 (1980) 325–333.

[20] J. Fleig, J. Maier, The impedance of ceramics with highly resistive grain boundaries: validity and limits of the brick layer model, J. Europ. Ceram. Soc. 19 (1999) 693–696.

[21] M. Maczka, E.T.G. Lutz, H.J. Verbeek, K. Oskam, A. Meijerink, J. Hanuza, M. Stuivinga, Spectroscopic studies of dynamically compacted monoclinic ZrO_2, J. Phys. Chem. Sol. 70 (1999) 1909–1914.

[22] M. Yashima, S. Sasaki, M. Kakihana, Y. Yagamuchi, H. Arashi, M. Yoshimura, Oxygen-induced structural-change of the tetragonal phase around the tetragonal-cubic phase-boundary in ZrO_2-$YO_{1.5}$ solid solutions, Acta Cryst. Sec. B Strcutural Sci. 50 (1994) 663–672.

[23] B. Akgenc, T. Cagin, Density functional theory of cubic zirconia and 6–15 mol% doped-yttria stabilized zirconia: structural and mechanical properties, Turk. J. Phys. 42 (2018) 223–231.

[24] H. Xiang, X. Lu, J. Li, J. Chen, Y. Zhou, Influence of carbon on phase stability of tetragonal ZrO_2, Ceram. Intern. 40 (2014) 5645–5651.

[25] S. Li, Z. Xie, D. An, C. Wei, P. Wang, L. Zhou, Zirconia ceramics consolidated by oscillatory pressure sintering and subsequent carburization, Ceram. Intern. 45 (2019) 9038–9042.

[26] T.Y. Luo, T.X. Liang, C.S. Li, Stabilization of cubic zirconia by carbon nanotubes, Mat. Sci. Eng. A366 (2004) 206–209.

[27] Y. Mo, T. Liu, X. Wang, J. Li, M. Yi, Microstructure, phase structure, and electrical properties of nitrided 3 mol% Y_2O_3 stabilized ZrO_2 (YSZ), Ceram. Int. 45 (3) (2019) 3680–3686.

[28] T. Hirata, E. Asari, M. Kitajima, Infrared and Raman-spectroscopy studies of ZrO_2 polymorphs doped with Y_2O_3 or CeO_2, J. Solid State Chem. 110 (1994) 201–207.

[29] C.G. Kontoyannis, M. Orkoula, Quantitative determination of the cubic, tetragonal and monoclinic phases in partially-stabilized zirconias by Raman-spectroscopy, J. Mater. Sci. 29 (1994) 5116–5320.

[30] M.T. Colomer, M. Maczka, Mixed conductivity, structural and microstructural characterization of titania-doped tetragonal yttria polycrystalline/titania-doped yttria stabilized zirconia composite anode matrices, J. Solid State Chem. 184 (2011) 365–372.

[31] M.T. Colomer, S. Díaz-Moreno, R. Boada, M. Maczka, J. Chaboy, Relatioships between structural and electrical properties in mixed conductors duplex materials in the ZrO_2-Y_2O_3-TiO_2 system, Phys. Rev. (B89) (2014) 094101(article number).

[32] T.A. Schaedler, O. Fabrichnaya, C.G. Levi, Phase equilibria in the TiO_2-$YO_{1.5}$-ZrO_2 system, J. Eur. Ceram. Soc. 28 (2008) 2509–2520.

[33] W. Cai, Q. Zhou, Y. Xie, J. Liu, G. Long, S. Cheng, M. Liu, A direct C solid oxide fuel cell operated on a plant derived biofuel with natural catalyst, Appl. Energy 179 (2016) 1232–1241.

[34] N. Shimodaira, A. Masui, Raman spectroscopy investigations of activated carbon materials, J. Appl. Phys. 92 (2002) 902–909.

[35] Y. Wang, D.C. Alsmeyer, R.L. McCreery, Raman spectroscopy of carbon materials-structural basis of observed spectra, Chem. Mater. 2 (1990) 557-553.

[36] C. Ciszak, M. Mermoux, G. Gutierrez, F. Leprêtre, C. Duriez, I. Popa, L. Fayette, S. Chevalier, Raman spectra analysis of zirconia thermally grown on Zircaloy substrates irradiated with heavy ion: effects of oxygen isotopic substitution, J. Raman Spectr. 50 (3) (2019) 425–435.

[37] A. Ben Ali, M.O. Awaleh, M. Leblanc, L.S. Smiri, V. Maisonneuve, S. Houlbert, Hydrothermal synthesis, crystal structure, thermal behaviour, IR and Raman spectroscopy of $Na_3Y(CO_3)_3{\cdot}6H_2O$, C. R. Chim. 7 (2004) 661–668.

[38] M.T. Colomer, C. Guglieri, S. Díaz-Moreno, M. Maczka, R. Boada, J. Chaboy, Effect of titania doping and sintering temperature on titanium local environment and electrical conductivity of YSZ, J. Alloy. Comp. 689 (2016) 512–524.

[39] I. Valov, I., R.A. De Souza, C.Z. Wang, A. Börger, C. Korte, M. Martin, K.D. Becker, J. Janek, Preparation of nitrogen-doped YSZ thin films by pulsed laser deposition and their characterization, J. Mater. Sci. 42 (2007) 1931–1941.

[40] J.F. Moulder, W.F. Stickle, P.E. Sobol, K.D. Bomben, Handbook of X-Ray Photoelectron Spectroscopy, Perkin-Elmer Corporation, Physical Electronics Division, Eden Prairie, Minn., USA, 1992.

[41] F. Parmigiani, L.E. Depero, L. Sangaletti, G. Samoggia, An XPS study of yttria-stabilized zirconia single-crystals, J. Electron. Spectrosc. Relat. Phenom. 63 (1993) 1–10.

[42] a) S. Biniak, G. Szymanski, J. Siedlewski, A. Swiatkowski, The characterization of activated carbons with oxygen and nitrogen surface groups, Carbon 35 (12) (1997) 1799–1810;
b) J.L. Figueiredo, M.F.R. Pereira, M.M.A. Freitas, J.J.M. Orfao, Modification of the surface chemistry of activated carbons, Carbon 37 (9) (1999) 1379–1389.

[43] (a) S. Yumitori, Correlation of C-1s chemical state intensities with the O-1s intensity in the XPS analysis of anodically oxidized glass-like carbon samples, J. Mat. Sci. 35 (2000) 139–146;
(b) (2004), A.V. Shchukarev, D.V. Korolvov, XPS studies of group IA carbonates, Cent. Eur. J. Chem. 2 (2) (2004) 347–362;
(c) D. Briggs, G. Beamson, Beamson, Primary and secondary oxygen-induced C 1sbinding energy shifts in X-ray photoelectron spectroscopy of polymers, Anal. Chem. (64) (1992) 1729–1736;
(d) C.M. Barnes, B.J. Kennedy, An X-ray photoelectron spectroscopic study of arenechromium tricarbonyl complexes at 170 K, J. Mol. Struct. (334) (1995) 233–240.

[44] T. Castner Jr ., G.S. Newell, W.C. Holton, C.P. Slichter, Note on the paramagnetic resonance of iron glasses, J. Chem. Phys. 32 (1960) 668–673.

[45] K.E. Swider, W.L. Worrell, Electron-paramagnetic-resonance of titanium impurities in reduced yttria-stabilized zirconia, J. Am. Ceram. Soc. 78 (1995) 961–964.

[46] J. Costantini, F. Beuneu, S. Morrison-Smith, R. Devanathan, W.J. Weber, Paramagnetic defects in electron-irradiated yttria stabilized zirconia: effect of yttria content, J. Appl. Phys. (110) (2011) 123506(article number).

[47] J. Costantini, F. Beuneu, Point defects induced in yttria stabilized zirconia by electron and swift heavy ion irradiations, J. Phys. Cond. Mat. (23) (2011) 115902.

[48] F. Pietrucci, M. Bernasconi, C. Di Valentin, F. Mauri, C.J. Pickard, EPR g-tensor of paramagnetic centers in yttria-stabilized zirconia from first-principles calculations, Phys. Rev. B (73) (2006) 134112.

[49] C.B. Azzoni, L. Bolis, A. Paleari, F. Scardina, Disorder-induced optical and paramagnetic properties in zirconium dioxide - role of low-symmetry crystal fields, J. Mag. Mag. Mat. 140 (1995) 175–176.

[50] J. Fleig, J. Maier, The impedance of ceramics with highly resistive grain boundaries: validity and limits of the brick layer model, J. Eur. Ceram. Soc. 19 (1999) 693–696.

[51] T. Van Dijk, A.J. Burgraaf, Grain boundary effects on ionic conductivity in ceramics $Gd_xZr_{1-x}O_{2-(x-2)}$ solid solutions, Phys. Status Solidi 63 (1981) 229–240.

[52] D. Chen, Z.J. Lin, H. Zhu, R.J. Kee, Percolation theory to predict effective properties of solid oxide fuel-cell composite electrodes, J. Power Sources 191 (2009) 240–252.

[53] C.M. Fernandes, A. Castela, F.M. Figueiredo, J.R. Frade, Microstructure-property relations in composite yttria-substituted zirconia solid electrolytes, Solid State Ion. 193 (2011) 52–59.

[54] P.S. Manning, J.D. Sirman, R.A. De Souza, J.A. Kilner, The kinetic of oxygen transport in 9.5 mol% single crystal yttria stabilised zirconia, Solid State Ion. 100 (1997) 1–10.

[55] M.T. Colomer, J.R. Jurado, Structure, microstructure, and mixed conduction of $[(ZrO_2)_{0.92}(Y_2O_3)_{0.08}](TiO_2)_{0.1}$, J. Solid State Chem. 165 (2002) 79–88.

[56] D. Skartmoutsos, A. Tsoga, A. Naoumidis, P. Nikolopoulos, 5 mol% TiO_2-doped Ni-YSZ anode cermets for solid oxide fuel cells, Solid State Ion. 135 (2000) 439–444.

[57] H.D. Tailor, J.L. Lyons, C.E. Dreyer, A. Janotti, C.G. Van, de Walle, Impact of nitrogen and carbon on defect equilibrium in ZrO_2, Acta Mater. 117 (2016) 286–292.

[58] I. Valov, V. Lein, T.-C. Rödel, S. Stork, M. Berendts, H.-D. Dogan, M. Wiemhöfer, Lerch Janek J., Ionic and electronic conductivity of nitrogen-doped YSZ single crystals, Solid State Ion. 180 (2009) 1463–1470.